Monthly Notices of the ROYAL ASTRONOMICAL SOCIETY

MNRAS **520,** 3696–3705 (2023) https://doi.org/10.1093/mnras/stad329
Advance Access publication 2023 February 2

Dynamical evolution of massive black hole pairs in the presence of spin-dependent radiative feedback

Francesco Bollati,[1,2]★ Alessandro Lupi,[2,3] Massimo Dotti[2,3,4] and Francesco Haardt[1,2,4]

[1]*DiSAT, Università degli Studi dell'Insubria, Via Valleggio 11, I-22100 Como, Italy*
[2]*INFN, Sezione di Milano-Bicocca, Piazza della Scienza 3, I-20126 Milano, Italy*
[3]*Dipartimento di Fisica G. Occhialini, Università di Milano-Bicocca, Piazza della Scienza 3, I-20126 Milano, Italy*
[4]*INAF, Osservatorio Astronomico di Brera, Via E. Bianchi 46, I-23807 Merate, Italy*

Accepted 2023 January 18. Received 2023 January 3; in original form 2022 July 11

ABSTRACT

The putative ubiquity of massive black holes (MBHs) at the centre of galaxies, and the hierarchical progress of structure formation along the cosmic history, together necessarily imply the existence of a large population of cosmic MBH binaries. Such systems are understood to be the loudest sources of gravitational waves at MHz frequencies, the regime that will be probed by the next Laser Interferometer Space Antenna. It has been proposed that the rate at which MBHs pair and then bind to form binaries is critically dependent upon the feedback exerted by the MBHs on the surrounding gaseous environment. Using the publicly available code GIZMO, we perform a suite of simulations aimed at studying the dynamics of an MBH pair embedded in a gaseous disc on ∼100-pc scale. By means of dedicated modules, we follow the dynamics of MBHs in the presence of different spin-dependent radiative feedback models, and compare the results to a benchmark case with no feedback at all. Our main finding is that feedback causes the secondary MBH to shrink its orbit at a reduced pace, when compared with models where feedback is absent. Moreover, such slower inspiral occurs on eccentric orbits, as feedback has the net effect of hampering the circularization process. Though idealized in many aspects, our study highlights and quantities the importance of including spin-dependent feedback recipes in hydrodynamic simulations of MBH pairs, and ultimately in assessing the cosmological coalescence rate of such systems in view of their detection through gravitational waves.

Key words: black hole physics – galaxies: nuclei – methods: numerical – quasars: supermassive black holes.

1. INTRODUCTION

Massive black hole (MBH) pairs are expected to form during galaxy mergers (Begelman, Blandford & Rees 1980, see De Rosa et al. 2019 for a recent review). During such dramatic interactions large amounts of gas are driven towards the centre of the forming remnant, either due to gravitational (e.g. Hernquist 1989; Barnes & Hernquist 1991, 1996; Mihos & Hernquist 1996) or hydrodynamical (Barnes 2002; Capelo & Dotti 2017; Blumenthal & Barnes 2018) torques. Such inflows result in the formation of a massive circum-nuclear (gaseous) disc (CND) commonly observed in the late stages of a galaxy merger (e.g. Sanders & Mirabel 1996; Downes & Solomon 1998).

Early numerical studies suggested that dynamical friction (DF) exerted by the dense CND on to the pairing MBHs may act in speeding up their orbital decay (Escala et al. 2005; Dotti, Colpi & Haardt 2006), at the same time circularizing the decaying orbits (Dotti et al. 2007). As a consequence, the delays between the galaxy merger completion and the formation of the MBH binary (MBHB) would be negligibly small even at high ($z \gtrsim 6$) redshifts, impacting the redshift distribution of the expected MBHB coalescences detectable by the future Laser Interferometer Space Antenna (LISA; eLISA Consortium et al. 2013). Furthermore, the drag towards circular corotation due to the CND-driven DF ensures small relative velocities between the pairing MBHs and the surrounding gas. This very fact enhances the probability of detecting dual active galactic nuclei (AGNs) on small scales ($\lesssim$1 kpc; Dotti et al. 2009), and promotes the prompt alignment of MBH spins with the orbital angular momentum (Dotti et al. 2010), hence decreasing the expected recoil velocities at coalescence (Bogdanović, Reynolds & Miller 2007). The net effect is an increase of the MBH occupation fraction at all redshifts (Volonteri, Gültekin & Dotti 2010).

The aforementioned studies, however, did not consider the possible feedback that accreting MBHs would exert on to the surrounding gas, altering its local properties and, therefore, its DF effect. Indeed, early indications of a sign reversal of the DF torque exerted by a rotating gaseous background affected by MBH feedback has been discussed on galactic scales by Sijacki, Springel & Haehnelt (2011). The authors found that recoiling MBHs on initially radial orbits tend to circularize corotating with the gaseous disc, and experience a fast orbital decay when AGN feedback is not included, while settle on counter-rotating orbits, resulting in higher relative velocities with respect to the gaseous environment and long orbital decay time-scales, when accretion-powered feedback is included.

This early claim has been numerically confirmed in the contexts of MBH pair dynamics on CND scales (see e.g. Souza Lima et al. 2017), where the pairing efficiency of the MBH is significantly reduced by

★ E-mail: fbollati@studenti.uninsubria.it

the AGN feedback and some small acceleration in the direction opposite to that of the standard DF is measured.[1] Similar indications have been found for stellar binary systems (Wang & Li 2022), planetary migration in protoplanetary discs (Masset 2017; Masset & Velasco Romero 2017) and have been discussed analytically in diverse contexts by Gruzinov, Levin & Matzner (2020).

In all the studies (both numerical and analytical) including AGN feedback mentioned above the energy or momentum injection has been assumed to be isotropic. However, at sufficiently small scales, the feedback may have significant deviations from isotropy, both in case of direct radiative feedback from the MBH accretion disc, as well as wind-mediated outflow or kinetic feedback from relativistic jets (see e.g. the discussion in Toyouchi et al. 2020, and references therein). An anisotropic feedback would increase significantly the complexity of the problem and, for some specific configurations, it may decrease the effect of feedback on to the local gaseous environment if the majority of the energy-momentum of the outflows escapes through a minimal-resistance path before altering the gas dynamics.

Here, we consider for the first time the impact of a spin-dependent radiative feedback on the dynamics of a MBH pair embedded in a CND, exploring different feedback models based on an anisotropic momentum injection in the gas. In particular, we couple the direction of the feedback with that of each MBH spin, evolving due to gas accretion following the prescription discussed in Cenci et al. 2021 and Sala et al. 2021, hereafter C21 and S21, respectively. In Section 2, we describe the model of spin-dependent feedback we adopt in our simulation suite. The specific set-up of our simulations is presented in Section 3, while results are discussed in Section 4. Finally, Section 5 is devoted to summary and concluding remarks.

2. MODEL

In this section, we review the model for MBH spin evolution and feedback implemented in GIZMO (Hopkins 2015) by C21 and S21.

The MBH particle is meant to represent a structured, subresolution system consisting of an MBH surrounded by an unresolved, warped accretion α-disc (Shakura & Sunyaev 1973). The MBH particle is completely characterized by its dynamical mass $M_{\bullet,\,\mathrm{dyn}}$, [2] whereas the subresolution, proper MBH (hereafter, simply the MBH) by its mass $M_\bullet$ and dimensionless spin-parameter $a = c|\boldsymbol{J}_\bullet|/GM_\bullet^2$, where $\boldsymbol{J}_\bullet$ is the MBH angular momentum, c the speed of light, and G the gravitational constant. The unresolved accretion disc is specified by its mass M_α, its total angular momentum $\boldsymbol{J}_\alpha$, and the accretion rate $\dot{M}_{\mathrm{acc}} = f_{\mathrm{Edd}}\dot{M}_{\mathrm{Edd}}$, where $\dot{M}_{\mathrm{Edd}} = 4\pi GM_\bullet m_{\mathrm{p}}/(\sigma_{\mathrm{T}}\eta c)$ is the Eddington accretion rate, m_{p} the proton mass, σ_{T} the Thomson scattering cross-section, and η the disc radiative efficiency. In general, $\boldsymbol{J}_\bullet$ and $\boldsymbol{J}_\alpha$ are misaligned, i.e. the α-disc is warped, with the inner region lying in the MBH equatorial plane and the outer part aligned with $\boldsymbol{J}_\alpha$ (Bardeen & Petterson 1975). The α-disc model employs prescriptions for the radial and vertical viscosity ν_1 and ν_2, which regulate, respectively, the accretion on to the MBH and the propagation of vertical perturbations. Both viscosities are expressed in terms of the Shakura & Sunyaev α-parameter (Shakura & Sunyaev 1973; Lodato & Pringle 2007).

Black hole (BH) and unresolved disc parameters are updated every MBH time-step according to analytical prescriptions that link the subresolution system to the resolved scales. The unresolved system parameters, in turn, are used to model the effects of MBH feedback on resolved scales. The coupling between resolved and unresolved scales is limited to those particles lying within the MBH smoothing kernel, which is defined as a spherical region centred on the MBH enclosing a given effective number of particles $N_{\mathrm{ngb},\,\bullet}$. In order to avoid coupling feedback on very large scales, the kernel size is capped at a maximum radius $R_{\bullet,\,\mathrm{max}}$. The aforementioned prescriptions have been implemented in GIZMO by C21 and S21, and their main features are summarized in the following.

2.1 Subgrid accretion and spin evolution

The time evolution of the MBH mass is governed by the accretion rate $\dot{M}_{\mathrm{acc}}$ and the accretion radiative efficiency η, whereas the mass of the unresolved disc feeding the MBH evolves according to the mass inflow $\dot{M}_{\mathrm{in}}$ from resolved scales, the mass outflow $\dot{M}_{\mathrm{w}}$, and $\dot{M}_{\mathrm{acc}}$ as

$$\dot{M}_\bullet = (1-\eta)\dot{M}_{\mathrm{acc}}, \tag{1}$$

$$\dot{M}_\alpha = \dot{M}_{\mathrm{in}} - \dot{M}_{\mathrm{acc}} - \dot{M}_{\mathrm{w}}. \tag{2}$$

Equations (1) and (2) are then used to update the masses of MBH and disc after a time-step Δt as $M_{\bullet,t+\Delta t} = M_{\bullet,t} + \dot{M}_{\bullet,t}\Delta t$ and $M_{\alpha,t+\Delta t} = M_{\alpha,t} + \dot{M}_{\alpha,t}\Delta t$. $\dot{M}_{\mathrm{in}}$, the mass inflow on to the MBH particle, is modelled as spherical accretion a la Bondi–Hoyle–Lyttleton [3](Hoyle & Lyttleton 1939; Bondi & Hoyle 1944; Bondi 1952), implemented by Springel, Di Matteo & Hernquist (2005) as

$$\dot{M}_{\mathrm{in}} = \frac{4\pi G^2 M_\bullet^2 \rho}{(c_{\mathrm{s}}^2 + |\boldsymbol{v}_\bullet - \boldsymbol{v}|^2)^{3/2}}, \tag{3}$$

where ρ, $\boldsymbol{v}$, and c_{s} are the gas density, velocity, and sound speed, respectively, computed as mass-weighted averages on the gas particles within the MBH smoothing kernel, and $\boldsymbol{v}_\bullet$ is the MBH velocity. In C21's implementation, the disc mass M_α is allowed to vary between a user-defined minimum value $M_{\alpha,\mathrm{seed}}$, which is reset in case M_α vanished due to accretion on to the MBH, and a maximum value set to prevent the unresolved disc from becoming self-gravitating.

$\dot{M}_{\mathrm{acc}}$ is self-consistently evolved according to the evolution of the subgrid quantities $\{\boldsymbol{J}_\bullet, \boldsymbol{J}_\alpha, \eta, f_{\mathrm{Edd}}\}$, which are updated at each MBH time-step. The time variation of the MBH angular momentum, $\dot{\boldsymbol{J}}_\bullet$, is determined by the angular momentum carried by the unresolved accreted gas at the innermost stable orbit (ISCO), which modifies the spin magnitude, and by the gravitomagnetic torque between the MBH spin and disc angular momentum, which tends to align the MBH spin to the total (i.e. MBH + disc) angular momentum (King et al. 2005; Fiacconi, Sijacki & Pringle 2018). Conservation of angular momentum implies $\dot{\boldsymbol{J}}_\alpha = -\dot{\boldsymbol{J}}_\bullet + \dot{\boldsymbol{J}}_{\mathrm{in}}$, where $\dot{\boldsymbol{J}}_{\mathrm{in}}$ is the angular momentum inflow from the resolved gas, i.e. $\dot{\boldsymbol{J}}_{\mathrm{in}} = \dot{M}_{\mathrm{in}}\Lambda_{\mathrm{in}}$, where Λ_{in} is the angular momentum per unit mass of the inflowing material (C21). Then, the MBH and disc angular momenta are updated as $\boldsymbol{J}_{\bullet,t+\Delta t} = \boldsymbol{J}_{\bullet,t} + \dot{\boldsymbol{J}}_{\bullet,t}\Delta t$ and $\boldsymbol{J}_{\alpha,t+\Delta t} = \boldsymbol{J}_{\alpha,t} + \dot{\boldsymbol{J}}_{\alpha,t}\Delta t$. The radiative

[1] See, however, Toyouchi et al. (2020) for an opposite indication when considering high densities ($\gtrsim 10^6$ cm^{-3}), large relative velocities ($\gtrsim 100$ km s^{-1}) between the BH and the gas, and the effect of dust in determining the extent of the region affected by feedback.

[2] The dynamical mass is that used in the computation of the gravitational force.

[3] We point out that the classical Bondi–Hoyle accretion we employ (equation 3) has the tendency to overestimate the accretion on the BH, as shown by Hopkins & Quataert (2011), Curtis & Sijacki (2016), and Tremmel et al. (2017).

efficiency η depends on the location of the ISCO which, in turn, is a function of the MBH spin parameter a, and is then consistently evolved. Finally, once the subgrid parameters are updated, $f_{\rm Edd}$ can be computed following the prescription by Fiacconi et al. (2018, see their equation 2), hence giving $\dot{M}_{\rm acc}$. In the scheme just described, the MBH time-step Δt is taken small enough to resolve the subgrid accretion and spin evolution and large enough to guarantee that the disc attains a steady-state warped profile, as assumed in our prescriptions.

The outflow rate $\dot{M}_{\rm w}$ is instead computed from the unresolved system parameters as

$$\dot{M}_{\rm w} v_{\rm w} = p L_{\rm bol}/c = p\eta c \dot{M}_{\rm acc}, \tag{4}$$

where $L_{\rm bol} = \eta \dot{M}_{\rm acc} c^2$ is the disc bolometric luminosity, $v_{\rm w}$ the wind speed, and p is the ratio between the wind and disc radiation momentum fluxes. Both $v_{\rm w}$ and p are free parameters of the model.

2.2 Stochastic feedback

The last quantity we need to evolve is the dynamical mass of the MBH particle. While $M_\bullet$ and M_α evolve smoothly over time, to keep under control the error made in mass conservation, $M_{\bullet,\,\rm dyn}$ is instead subject to a stochastic evolution (Springel et al. 2005). This is modelled via a stochastic selection of gas particles within the MBH kernel, whose mass is reduced by a fraction f, which is added to the MBH dynamical mass. The remaining $(1-f)$ fraction of the selected particles is then kicked outwards with a velocity $v_{\rm w}$ along specific directions that depend on the chosen feedback model, thus concurring to form the resolved MBH-driven wind. The fraction f is defined as $f = 1 - \dot{M}_{\rm w}\Delta t/(\sum_k^N m_k)$, where m_k is the mass of the kth gas particle among the N selected. This choice of f guarantees that the entire amount of ejected mass $(1-f)\sum^N m_k$ is, at every time-step, equal to $\dot{M}_{\rm w}\Delta t$. The probabilities to select particles are chosen to guarantee that, on average, the mass transferred to $M_{\bullet,\,\rm dyn}$ is $f\sum_k^N m_k \simeq M_{\bullet,t+\Delta t} + M_{\alpha,t+\Delta t} - M_{\bullet,t} - M_{\alpha,t}$ (see S21 for further details).[4]

By varying the kick direction, the outflow anisotropy can be tuned to reproduce different feedback mechanisms. In particular, the outflow can be either modelled as an isotropic wind, where the selected particles receive a kick along the radial direction, as a collimated jet parallel to the gas angular momentum, as implemented by Anglés-Alcázar et al. (2017), or it can be assumed to have a biconical shape, as implemented by S21. In the latter case, the kick direction is randomly sampled within a cone of given semi-aperture $\theta_{\rm bic}$, with the cone axis either fixed in time or consistently evolved during the simulation (e.g. parallel to the MBH spin).

3. NUMERICAL SIMULATION SET-UP

In order to simulate the dynamics of MBH pairs in presence of spin-dependent radiative feedback, in this work we employed the publicly available N-body, mesh-less hydrodynamic code GIZMO (Hopkins 2015) supplied with the implementations by C21 and S21, presented in Sections 2.1 and 2.2. This enabled us to investigate the role of feedback in the orbital evolution of MBH pairs placed in a gaseous and stellar environment. Simulations were run on the CINECA cluster MARCONI 100.

Here, we discuss the set-up of the numerical simulations we performed, consisting in a MBH pair embedded in a gaseous CND and in a stellar bulge. The initial conditions have been created by first initializing the stellar and gaseous components in dynamical equilibrium with the primary MBH (placed at the centre of the system) and by subsequently adding the secondary MBH to the relaxed system. We achieved the first step by using the publicly available code GD_BASIC (Lupi, Haardt & Dotti 2015), building up a 'bulge + CND + primary' (BCP hereinafter) system characterized by:

(i) a spherical stellar bulge described by an Hernquist (1990) profile

$$\rho_{\rm b}(r) = \frac{M_\star}{2\pi}\frac{r_\star}{r(r+r_\star)^3}, \tag{5}$$

where r is the spherical radial coordiante, $M_\star = 5\times10^8$ M$_\odot$ the total bulge mass, and $r_\star = 100$ pc the bulge scale radius;

(ii) a rotationally supported exponential disc in vertical hydrostatic equilibrium whose surface density profile is

$$\Sigma(R) = \frac{M_{\rm d}}{2\pi R_{\rm d}^2} e^{-R/R_{\rm d}}, \tag{6}$$

where R is the cylindrical radial coordinate, $R_{\rm d} = 50$ pc the disc scale radius, and $M_{\rm d} = 10^8$ M$_\odot$ the disc total mass;

(iii) a primary MBH with dynamical mass $M_1 = 10^7$ M$_\odot$ at rest in the centre of the system.

The stellar and gaseous components are sampled by $N_\star = 5\times10^6$ and $N_{\rm d} = 10^6$ particles, respectively, corresponding to a mass resolution of 10^2 M$_\odot$ for both. The spatial resolution is determined by the Plummer equivalent gravitational softening $\epsilon_{\rm soft}$. For stellar and MBH particles it is fixed at 0.1 and 0.33 pc, respectively, while for gas particles it is adaptively set equal to the hydrodynamic kernel size, i.e. the radius encompassing an effective number of neighbours $N_{\rm ngb} = 32$, down to a minimum allowed value $\epsilon_{\rm soft,\ min} = 0.1$. The gas particles are also initialized with a uniform temperature $T = 2\times10^4$ K, assuming an ideal equation of state with adiabatic index $\gamma = 5/3$. Once created, in order to relax the system, the BCP is evolved for 20 Myr, corresponding to $\sim$6 orbits at $R_{\rm d}$ and $\sim$3.22 orbits at $r_\star$.

After relaxation, we introduced a secondary MBH with dynamical mass M_2 in the disc plane ($z = 0$) at a separation of 80 pc from the BCP centre of mass,[5] producing different initial conditions depending on the initial mass ratio $q = M_2/M_1$ and initial eccentricity e. These initial conditions are aimed at modelling the final stages of the MBHs DF-driven inspiral that brings the MBHs separation from kpc to pc scales (Mayer et al. 2007; Amaro-Seoane et al. 2022). In our fiducial simulations (indicated with **f**) we initialized the secondary with $q = 1/2$ and $e = 0$ (w.r.t. the centre of mass of the BCP) and initial velocity $\boldsymbol{v}_2(t=0) = \sqrt{R|{\rm d}\Phi/{\rm d}R|}\,\hat{\varphi}$, where $\hat{\varphi}$ is the azimuthal unit vector and Φ is the gravitational potential of the BCP. Compared with this fiducial run, simulations labelled as **q** all have a lower mass ratio ($q = 1/6$), simulations labelled as **e** have a non-vanishing initial radial velocity component that sets the initial eccentricity to $e = 0.5$ (see Table 1). For each of these three initial set-ups (**f, q**, and **e**) we performed four simulations considering different feedback models: (i) the case without feedback (labelled as **nofb**), (ii) isotropic feedback (labelled as **iso**), (iii) biconical feedback with the cone axis

[4] In order to ensure that the dynamical mass follows on average the physical mass, when $M_{\bullet,\,t+\Delta t} < M_{\bullet,\,\rm dyn}$ we only change the momentum of the selected particles, and leave the MBH dynamical mass unchanged.

[5] After adding the secondary MBH, we also shifted the positions and velocities of all the particles in order to move the centre of mass of the BCP + secondary system at rest in the origin.

Table 1. Summary of the parameters adopted in our simulations. Top: parameters that vary across our simulation suite. The following parameters are the same for all runs: for feedback launching $\theta_{\rm bic} = 45^\circ$, $p = 1$, and $v_{\rm w} = 500\ {\rm km\,s^{-1}}$ and for the subgrid system $a = 0.5$, $f_{\rm Edd} = 0.01$, $M_\alpha/M_\bullet = 0.005$, and $\alpha = 0.1$. Our choice of M_α guarantees that the initial disc mass is smaller than the disc self-gravitating mass $M_{\rm sg}$. Bottom: gravitational softening for the different components.

	q	e	$\frac{J_\alpha}{J_\bullet}$	$\frac{M_\alpha}{M_{\rm sg}}$	$R_{\bullet,\,\rm max}$ (pc)
f	1/2	0	2.85	0.52	3
q	1/6	0	4.84	0.40	1
e	1/2	0.5	2.85	0.52	3
Type	$\epsilon_{\rm soft}$ (pc)				
Gas	0.1				
Bulge	0.1				
MBH	0.33				

fixed and parallel to the vertical direction $\hat{z}$ (labelled as **z**), and (iv) biconical feedback with the cone axis aligned to the evolving MBH spin direction (labelled as **a**). In the latter two cases, we fixed $\theta_{\rm bic} = 45^\circ$ and, whenever feedback is present, we used $v_{\rm w} = 500\ {\rm km\,s^{-1}}$ and $p = 1$, i.e. the radiation momentum flux is entirely transferred to the wind. Our complete simulation suite therefore comprises a total of 12 runs.

We remark that the modules for subgrid accretion plus spin-evolution and stochastic feedback (if present) are switched on for the secondary MBH only. This means we are considering the impact of feedback from the secondary on its own dynamics without accounting for the possible effects the feedback from the primary MBH may have on the secondary one. This is justified by the fact that we are in a regime where the relative separations of the two MBHs is large compared with the local regions possibly affected by feedback.

In all simulations, we initialize the secondary MBH mass as $M_\bullet = M_2/1.005$, $M_\alpha = 0.005 M_\bullet$, such that $M_\bullet + M_\alpha = M_2 (\equiv M_{\bullet,\,\rm dyn})$. The disc angular momentum direction is along the z-axis, while the initial MBH spin is 'flipped downwards' at an angle $5\pi/6$, with magnitude $a = 0.5$. The Eddington ratio is set at $f_{\rm Edd} = 0.01$, which together with the other subgrid parameters constrains the value of $J_\alpha/J_\bullet$ (equation 5 in C21). Finally, we use $N_{\bullet,\,\rm ngb} = 3N_{\rm ngb}$.

4. RESULTS

We discuss now the outcome of the simulations we carried out, starting from **f**-simulations in Section 4.1. In the subsequent sections we perform the same analysis for **e**- and **q**-simulations.

4.1 f-simulations

4.1.1 Qualitative analysis

The time evolution of the MBH separation and M_2 eccentricity is shown in Figs 1 and 2, respectively, for the four tested different feedback models in **f**-simulations. Overall, we observe that in presence of feedback the time-scale of orbital decay of M_2 is larger and the orbits tend to develop higher eccentricities. We can get some insights into such behaviour from the evolution of the torques acting on M_2 shown in Fig. 3. The torque in **f_nofb** is always negative, indicating that efficient DF is acting on M_2, hence causing a net loss of angular momentum and energy, leading to rapid inspiral towards M_1. On the other hand, switching feedback on, the torques on M_2 can become positive, indicating in these phases an inefficient (or even

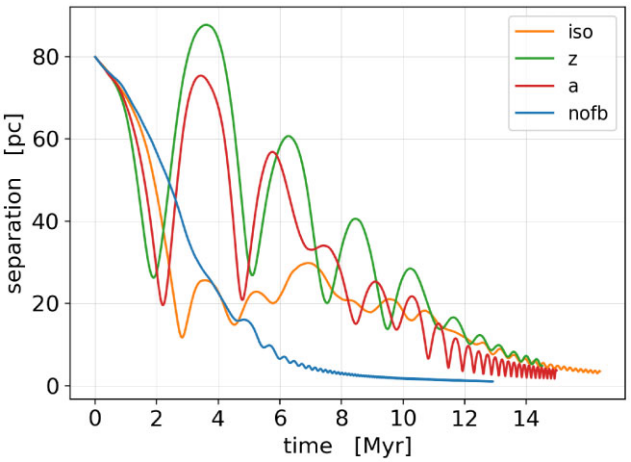

Figure 1. Time evolution of the MBH separation in **f**-simulations.

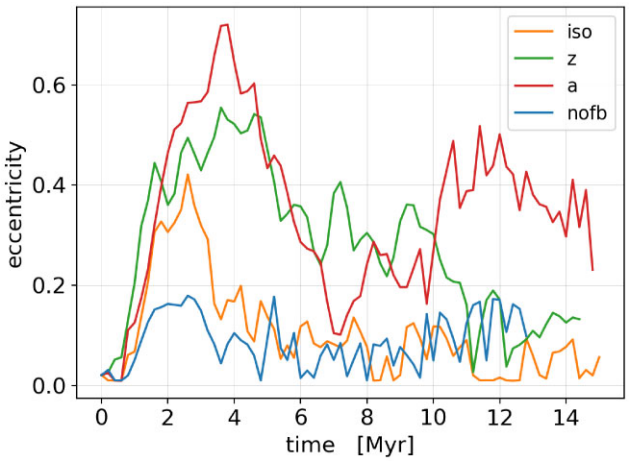

Figure 2. Time evolution of the eccentricity of M_2 in **f**-simulations.

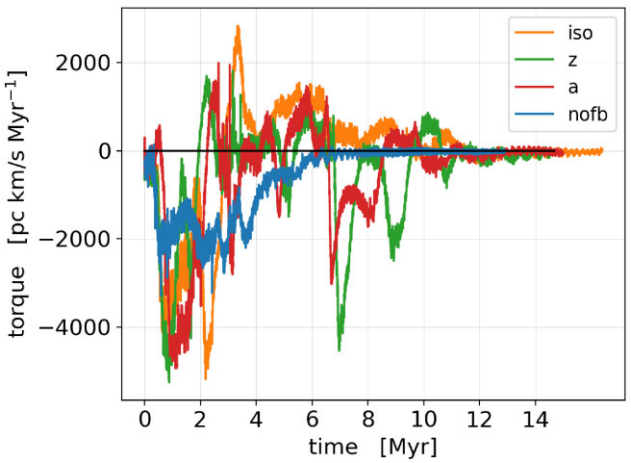

Figure 3. Time evolution of the z-component of the total torque acting on M_2 in **f**-simulations.

reversed) DF, i.e. a positive acceleration, and hence an orbital decay at slower pace.

In more details, as shown in Fig. 3, the z-component of the torque acting on M_2 initially quickly drops to negative values. In this phase, lasting ∼2 Myr, in **f_iso, f_z** and **f_a** the torque is twice as large (in magnitude) than that in **f_nofb**, i.e. DF is initially enhanced by feedback processes. In all cases, the initial larger loss of angular momentum in the presence of feedback is accompanied by an increase in eccentricity (Fig. 2). Later on, the z-component of the torque becomes positive, i.e. the angular momentum increases, something not seen in **f_nofb**, where the torque is always negative.

We notice (see Fig. 3) that in **f_iso** the initial negative torque phase is prolonged slightly further compared with the other feedback simulations, causing the first pericentre to be closer to M_1 (∼10 pc), and to occur at a later time (∼3 Myr). Because of such longer journey to the pericentre, M_2 loses more energy compared with the **f_z** and **f_a** cases, consequently acquiring a smaller eccentricity, $e \simeq 0.1$, with the separation stalled around ≃20 pc for the subsequent ≃10 Myr. In this phase, M_2 is subject to a net positive torque that traces a 'reversed' DF. Then, the system enters a further phase in which the separation decreases again.

In **f_z**, the eccentricity grows to $e \simeq 0.5$ when M_2 reaches the first apocentre, and then slowly decays. We also observe that the first apocentre is located at a distance larger than the initial MBHs separation, signalling a net gain of energy. In **f_a**, M_2 orbits follow a similar trend, with an initial rapid rise in eccentricity followed by a slower circularization along M_2 orbital decay.

Finally, we see that the two MBHs form a binary, at ∼5 Myr in **f_nofb**, and between 10 and 12 Myr in feedback simulations. We comment the convergence of these results in the Appendix A.

4.1.2 *Quantitative analysis*

DF is generally attributed to the many two-body encounters between a massive object (M_2 in the present context) and background stars (Chandrasekhar 1943). In the case of a gaseous background, DF can be understood in terms of the gravitational interaction between M_2 and the density wake generated by its motion in the gaseous background. In fact, the relative motion of M_2 with respect to the background creates an overdensity on the side opposite to the relative velocity between M_2 and fluid. The gaseous DF acts in all respect as a non-conservative drag force (Ostriker 1999). However, the gas around the MBH can be (partially) blown away by radiative feedback, thus hampering the formation of the density wake itself. The density enhancement trailing M_2 is, in this case, replaced by an underdensity, we refer to it as 'density bubble', affecting M_2 dynamics in a decisive manner.

In order to quantify the effects the radiative feedback has on M_2 orbital decay, we introduce an 'anisotropy vector' defined as

$$\boldsymbol{A} \equiv \sum_i m_i \, w(r_i) \frac{\boldsymbol{r}_i}{r_i}. \tag{7}$$

Here, the sum is intended over all particles (with mass m_i and position vector $\boldsymbol{r}_i$ in the CND plane centred in M_2) within a distance from M_2 equal to the minimum between 30 pc and the MBHs separation. Each particle is weighted by the force softening function implemented in GIZMO, w (see Appendix B). As $\boldsymbol{A}$ evolves in time through coordinates $\boldsymbol{r}_i$, we consider the (normalized) difference $\Delta\boldsymbol{A} \equiv \boldsymbol{A}_0 - \boldsymbol{A}$, where $\boldsymbol{A}_0$ is the anisotropy vector computed by considering, at each time, the current M_2 position but the initial distribution of gas. This allows us to quantify the time evolution of the anisotropy due to the MBH–gas interaction independently of any possible anisotropy already present at the beginning of the simulation.[6] The direction of $\Delta\boldsymbol{A}$ indicates the axis along which the anisotropy develops, pointing towards the lower density side. Therefore, in the presence of feedback, $\Delta\boldsymbol{A}$ indicates the bubble location, while, in absence of feedback, $\Delta\boldsymbol{A}$ points in the direction opposite to the overdensity wake. Fig. 4 shows $\Delta\boldsymbol{A}$ in a snapshot of **f_iso**.

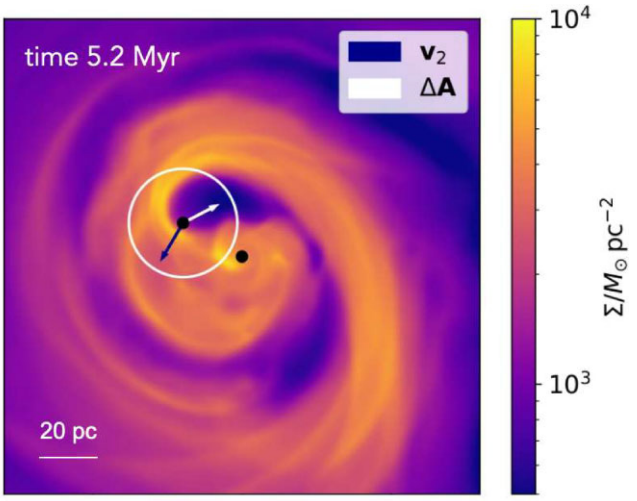

Figure 4. The surface density Σ (in $M_\odot$ pc^{-2}) in a snapshot of run **f_iso**. The two black dots indicate the positions of the MBHs. The white circle bounds the region around M_2 used to define the anisotropy vector $\boldsymbol{A}$, indicated by the white arrow. The dark-blue arrow indicates $\boldsymbol{v}_2$, the M_2 velocity.

If we now consider $A_2 \equiv \Delta\boldsymbol{A} \cdot \boldsymbol{v}_2$, i.e. the projection of $\Delta\boldsymbol{A}$ along the M_2 velocity vector $\boldsymbol{v}_2$, we see that a positive value of A_2 would indicate that the bubble lies in front of M_2 (or that the overdensity lies behind M_2 in **nofb**-type simulations). In this case the gas distribution around M_2 exerts a gravitational force opposite to the direction of motion, resulting in an efficient DF. On the other hand, the underdense bubble lies behind M_2 for negative values of A_2, thus imparting a net acceleration to M_2 (see Fig. 4).

We can now use A_2 to interpret the dynamics of M_2 described in Section 4.1. Fig. 5 shows the evolution of A_2 for all four **f**-simulations. First, we observe that in **nofb** A_2 is positive, meaning that an overdensity is present behind the MBH. This produces a negative torque that forces M_2 to rapidly inspiral towards M_1. Conversely, when feedback is switched on, A_2 has initially positive values (and larger compared with **nofb**), suggesting that DF is enhanced in the early inspiral phase by the action of feedback (see. Section 4.1). In Fig. 6, we compare snapshots taken at the same time (2 Myr after the start of the simulation) for **f_nofb** and **f_iso**. In the first case, the formation of a spiral wave in the disc is accompanied by the presence of a moderately low-density region in front of M_2. When feedback is included, this region exerts a weaker resistance to the gas particles blown away by radiation pressure, allowing the bubble to expand in such direction. As a consequence, the gas surrounding M_2 exhibits a larger anisotropy, i.e. an initially larger value of A_2 corresponding to a larger negative torque. From Fig. 5, we also notice that in **f_iso** the phase during which the bubble lies in front of M_2 ($A_2 > 0$) lasts longer compared with the other feedback models, consistently with the more prolonged negative torque observed in Fig. 3. Indeed,

[6] We note that this choice would be slightly affected by the Poisson noise in the initial distribution of the gas.

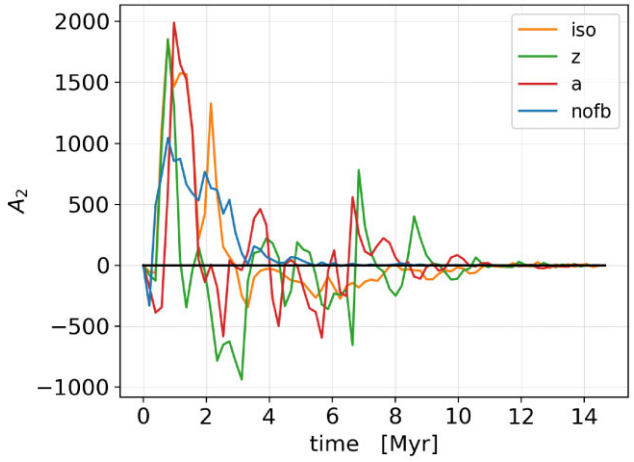

Figure 5. Time evolution of the anisotropy projection A_2 in **f**-simulations.

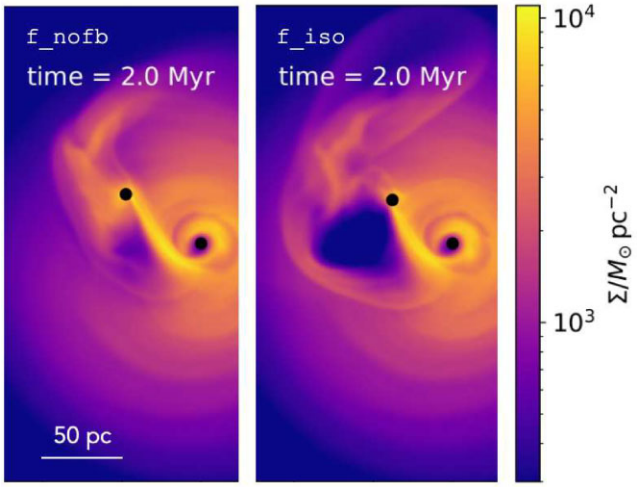

Figure 6. Two snapshots at time $t = 2$ Myr of runs **f_nofb** (left-hand panel) and **f_iso** (right-hand panel).

isotropic feedback is more efficient than anisotropic models (**z** and **a**) in keeping the low-density bubble 'open', as particles are more easily kicked in the CND plane (where the gas density is higher), hence more likely able to prolong the dynamical effect of the preceding bubble.

After the initial preceding-bubble ($A_2 > 0$) phase, all simulations with feedback show a drop and eventually a sign change in A_2. This turning point approximately corresponds to M_2 reaching the pericentre. Indeed, as M_2 approaches the pericentre, its orbital speed exceeds that of the gas, overtaking the bubble which then lags behind. In this configuration, A_2 is negative, and M_2 accelerates, increasing its eccentricity. In particular, **f_z** displays the most negative value of A_2, implying that M_2 receives more energy in the process. In this case, M_2 reaches the first apocentre at a distance which is actually larger than the initial MBHs separation. In **f_iso** A_2 remains negative in the time interval $\simeq$[3–10] Myr, i.e. M_2 keeps being accelerated by the trailing bubble. Interestingly, in our simulations such feedback-driven acceleration is approximately balanced by stellar DF, and the semimajor axis remains approximately constant during this phase (see Fig. 4 for a snapshot from this evolutionary phase).

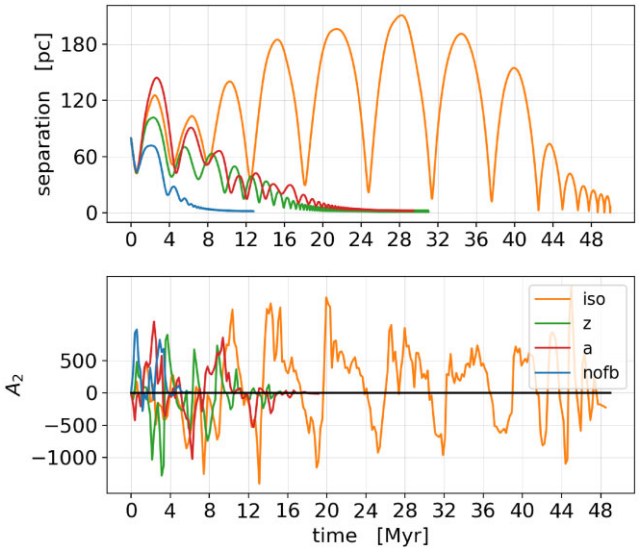

Figure 7. Time evolution of the MBHs separation (top panel) and anisotropy projection A_2 (bottom panel) in **e**-simulations.

4.2 e-simulations

M_2 orbits corresponding to simulations with an eccentric initial condition are shown in Fig. 7 (top panel), together with the evolution of A_2 (bottom panel). In **e_nofb**, the MBH separation rapidly decays and orbit circularizes. This occurs as M_2 produces a density wake on the side opposite to the relative velocity between itself and the fluid. Therefore, since the orbital speed of M_2 close to the pericentre is larger than the local gas rotational velocity, the wake lags behind and M_2 slows down. On the other hand, near the apocentre the MBH velocity is smaller than the disc one and the wake is dragged in front of M_2, increasing its angular momentum and accelerating it. The combination of these two opposite effects at pericentre and apocentre results in orbit circularization (Dotti et al. 2007; Bonetti et al. 2020). When radiative feedback is switched on, the density wake is somewhat destroyed and a low-density bubble is created instead. Circularization is thus less effective, as it can be seen in Fig. 7, top panel, in the cases of **e_z** and **e_a**. In **e_iso**, because of the stronger impact of feedback on the surrounding gas, the density wake is more efficiently blown away and replaced by a low-density bubble, which now follows the same trend of the wake in **e_nofb**, but with the opposite gravitational effect. Therefore, at apocentre the bubble falls in front of the MBH, enhancing DF, while at pericentre it trails behind, accelerating the MBH, with the net effect of increasing the eccentricity. This behaviour is illustrated in Fig. 7 where, in **e_iso**, M_2 develops relatively high ($0.5 \lesssim e \lesssim 0.9$) eccentricities. Correspondingly, A_2 is positive (i.e. bubble lies ahead) at apocentre and negative (i.e. bubble lies behind) at pericentre, supporting our interpretation (see Fig. 7, bottom panel).

4.3 q-simulations

Fig. 8 illustrates the time evolution of MBH separation and of A_2 is illustrated in the case of a $q = 1/6$ mass ratio. Overall, we can see that, in the feedback runs, M_2 orbits differ more from the **nofb** case, compared with what we have seen in **f** and **e** cases. The evolution of the orbital separation is again associated with the effects induced by the feedback. In **q_z**, M_2 eccentricity increases up to $\sim$0.5 in the first $\sim$15 Myr, with the growth associated to an oscillating

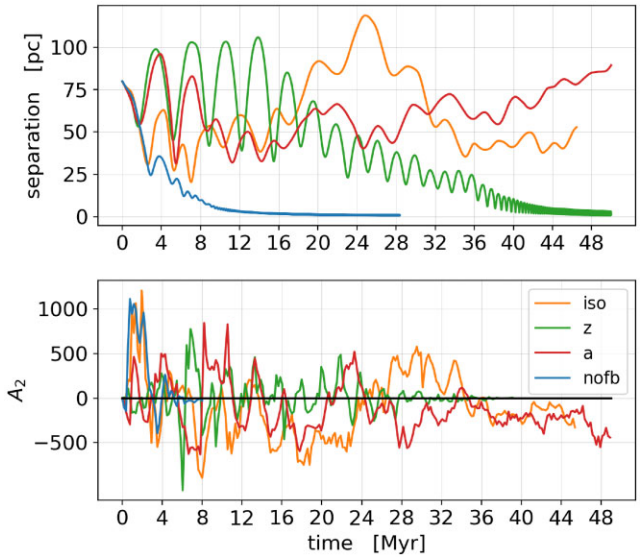

Figure 8. Same as Fig. 7 but for **q**-simulations.

behaviour of A_2, positive at apocentre and negative at pericentre, as discussed in Section 4.2. By contrast, in **q_iso** and **q_a**, M_2 orbits are quasi-circular, with an average eccentricity $e \lesssim 0.1$. In these cases, M_2 orbit is not going to shrink appreciably by the end of the simulation. Again, the increasing/decreasing trends of the MBHs separation due to positive/negative torques are linked to feedback, as they correspond, respectively, to negative/positive values of A_2 (Fig. 8, bottom).

Interestingly, in **q_a**, after $\simeq$25 Myr the distance of M_2 from M_1 shows, on average, a slightly increasing trend. We can explain this behaviour as follows: Due to the pressure gradient in the disc, the gas circular velocity is smaller than that of the MBH, settled on a quasi-circular orbit, and hence the bubble created in the disc by feedback is overtaken by the MBH, favouring its acceleration. In principle, this acceleration can be balanced by stellar DF, that concurs in maintaining M_2 on a quasi-circular orbit.

4.4 Angular pattern

In our analysis, we have shown through the quantity A_2 how radiative feedback is linked to the torques experienced by M_2, and how it can have an impact on orbital eccentricity and decay time-scale. Here, we will discuss in a more quantitative way the relation existing between gas density perturbations due to feedback and the orbital decay time-scale and eccentricity.

If we consider the angle θ between $\Delta\boldsymbol{A}$ and $\boldsymbol{v}_2$, we do see that in the absence of feedback M_2 creates a trailing density wake, i.e. $\Delta\boldsymbol{A}$ tends to be directed parallel to $\boldsymbol{v}_2$, resulting in $\theta \lesssim \pi/2$. On the other hand, when feedback effects are considered, the low-density bubble in the disc can be either trailing or leading with respect to M_2, depending on the relative velocity between the disc and M_2. This corresponds to $\theta \gtrsim \pi/2$ and $\theta \lesssim \pi/2$, respectively.

For all simulations, we follow the time evolution of θ, and compute its weighted probability distribution. In practice, any occurrence of a given angle is weighted with the current value of $|\Delta\boldsymbol{A}|$, and the resulting frequency distribution of θ is then normalized. Results are shown in Fig. 9 for **f** simulations (the cases **q** and **e** are reported in Appendix C). As expected, the distribution in **nofb** is peaked at small angles ($\lesssim\pi/2$), whereas the feedback cases exhibit much more spread

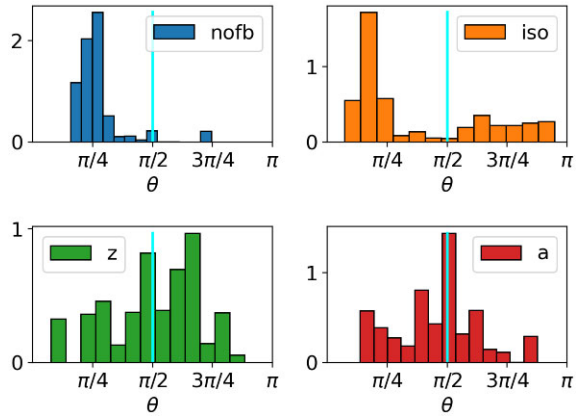

Figure 9. Probability distribution of the (weighted) angle θ between the anisotropy difference $\Delta\boldsymbol{A}$ and M_2 velocity $\boldsymbol{v}_2$ (see text for details) in the **f**-simulations.

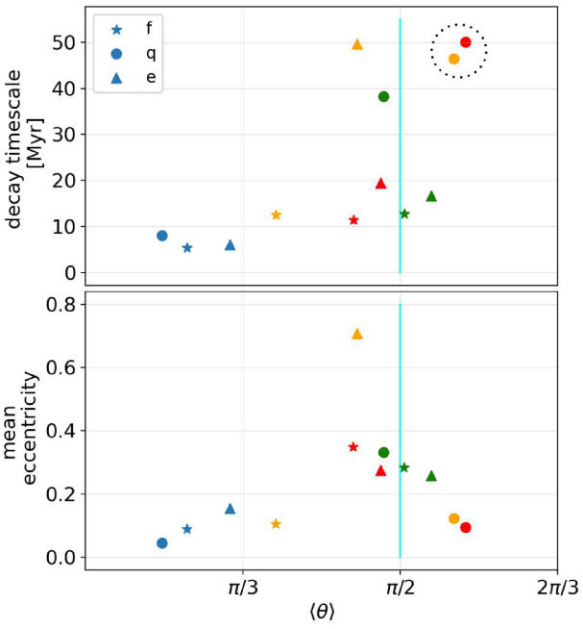

Figure 10. Top panel: The decay time-scale of M_2 versus the mean value of the angle θ between the anisotropy difference $\Delta\boldsymbol{A}$ and M_2 velocity $\boldsymbol{v}_2$, for the entire simulation suite. The decay time is estimated as the time that the semimajor axis of M_2 takes to reach an orbital distance to M_1 of 10 pc. The different colours label the different type of feedback with the same legend of previous figures. Note that for the two runs in the dotted circle (**q_a** and **q_z**) the time indicated is the stop time of the simulation, as in these two cases M_2 did not reach an orbital separation of 10 pc within the simulation time. Bottom panel: The mean eccentricity of M_2 versus the mean of θ. The legend is the same as in top panel.

values, across the entire range. In particular, the more the peak of the distribution shifts to larger values, the more frequently the secondary will be accelerated by feedback, making DF inefficient. Therefore we consider $\langle\theta\rangle$, the mean of θ, as a proxy for DF efficiency and, for each simulation, we compare its value with the orbital decay time-scale and the mean eccentricity.

In Fig. 10 (top panel), we plot $\langle\theta\rangle$ against the orbital decay time-scale, defined here as the time required by M_2 to reach an orbital semimajor axis $<$10 pc. Simulations without feedback present lower mean values of θ and lower values of decaying time-scale, while

both quantities are larger in feedback simulations, confirming that a feedback-induced trailing bubble delays the inspiral of M_2 towards M_1.

In particular, if we compare **f** and **q** simulations, both with initial circular orbits but different mass ratios, we observe that by lowering the mass ratio by a factor of 1/3 (i.e. moving from **f** to **q**) the decay time-scale is significantly delayed. This indicates that feedback is more likely to affect lighter MBHs dynamics, or, in other words, that the feedback accelerating force has a softer scaling with the perturber mass M compared with the DF force (which is $\propto M^2$). This is consistent with Gruzinov et al. (2020) and Li et al. (2020), who showed that the feedback-induced force acting on a perturber moving in a homogeneous medium scales as $\propto M^{3/2}$.

Similarly, in Fig. 10 (bottom panel) we compare $\langle\theta\rangle$ with the mean eccentricity. In the absence of feedback, DF is efficient and both $\langle\theta\rangle$ and mean eccentricity are small (<0.2), even for **e_nofb**, which started eccentric. On the other hand, when feedback is turned on, the majority of simulations exhibits excited eccentricities (or hindered circularization, as in **e_z** or **e_a**). By contrast, in three cases (**f_iso**, **q_iso**, and **q_z**), the secondary mean eccentricity remains small ($\sim$0.1), comparable with those found without feedback. The reason behind this different behaviour is that these simulations are characterized by prolonged stages of trailing bubbles in which feedback acceleration is counteracted by stellar DF.

5 SUMMARY AND CONCLUSIONS

Using the publicly available code GIZMO, we have run a suite of simulations aimed at studying the dynamics of an MBH pair embedded in a gaseous CND. By means of dedicated subresolution prescriptions, we could model the dynamics in the presence of spin-dependent feedback, and compare results obtained with different feedback models, and to a benchmark case with no feedback at all. Overall, we observed that feedback significantly alters the MBHs dynamics and different feedback models produce large differences in the orbital evolution of the MBH pair.

Our results can be summarized as follows:

(i) Feedback can both raise and suppress DF with the net effect of delaying the shrinking time-scale of an MBH pair. This very fact bears important consequences when we are to model the cosmic population of MBHBs, and their detectability via electromagnetic *and* gravitational waves;

(ii) Feedback has also a relevant effect on the eccentricity of MBHs orbits, exciting it or weakening the circularization process. Again, this fact is relevant for an assessment of the properties of MBH pairs as a cosmological population;

(iii) Finally, the effect of feedback on the dynamics of MBH pairs is more pronounced for decreasing mass ratios.

Our results then highlight that MBHs' dynamics strongly depends on the feedback model assumed, i.e. whether we are considering isotropic or anisotropic feedback, with fixed or spin-dependent collimation axis. It is therefore crucial to model the anisotropy and direction of feedback consistently with the MBH spin, which, in turn, evolves according to the accretion on the MBH, in order to reliable assess the role of feedback in the evolution of MBH pairs. This is the only way to consistently capture the interplay between feeding and feedback, allowing a proper modelling of MBHs pairing, which is essential in view of forthcoming low-frequency gravitational waves missions such as LISA (eLISA Consortium et al. 2013).

Due to our simplified modelling, a number of caveats that we have to keep in mind when interpreting our results do exist. Specifically:

(i) Our analysis is limited to coplanar orbits, an assumption justified by the fact that both the CND and the MBHs inherit their angular momentum from the parent merging galaxies, leading to orbits likely lying in the same orbital plane (Colpi et al. 2007; Mayer et al. 2007). None the less, if coplanarity is not guaranteed, the pair inspiral is initially driven mainly by the DF exerted by the stellar bulge, while gaseous DF dominates once the MBHs separation becomes small enough that the MBHs spend most of their time in the disc (Escala et al. 2005). As a consequence, for non-coplanar orbits, we expect the feedback-induced eccentricity and delayed decay to be initially negligible and to become progressively more important as the pair shrinks and gets closer to binary formation.

(ii) In **z** and **a** feedback models, the anisotropy has been realized by kicking the gas particles within a well-defined cone, as if the driving radiation emitted by the subgrid disc had a step-like angular pattern, non-vanishing within the cone. In reality, the disc radiation angular pattern can be described with a continuous function which depends upon the MBH spin (Campitiello et al. 2018) and therefore evolves with it;

(iii) We have not included any form of cooling in the simulations. Cooling can potentially make the low-density bubbles expand as momentum-driven structures, hence more slowly, since the shock wind thermal energy that swells the bubbles is radiated away. Therefore, cooling may have an impact on the bubbles formation/expansion which, in turn, may reflect on the MBH dynamics;

(iv) The MBH wind has been simulated via injection of kinetic energy only, by adding momentum to gas particles within the MBH kernel. The lack of thermal energy injection tends to postpone the wind thermalization (Costa, Pakmor & Springel 2020), thus speeding up the bubble expansion, which, again, may affect the MBH dynamics;

(v) If the region within $R_{\bullet,\,\mathrm{max}}$ (the maximum MBH kernel size) is emptied, i.e. a sufficiently large low-density bubble is formed around the MBH, feedback is artificially shut off since no more particles are eligible to be kicked, until the MBH kernel is refilled. This can weaken bubbles expansion thus influencing the MBH orbital evolution.

In a paper in preparation we are going to refine our recipes for feedback implementation, in order to overcome most of the aforementioned limitations. More in detail, our new implementation is based on spawning AGN wind gas particles (Torrey et al. 2020) from the subgrid accretion disc, such that their angular mass distribution follows the same angular pattern of the accretion disc luminosity (Campitiello et al. 2018), in this way linking the wind anisotropy, and not only its direction, to the MBH spin. Then, wind particles are kicked outward radially at fixed velocity and by interacting with the surrounding gas particles they generate an anisotropic outflow. We expect this different feedback model to affect the formation of low-density bubbles and hence the MBHs inspiral rates, compared with this work. Indeed, on the one hand this new model would tend to produce wider bubbles because feedback is not artificially shut off once gas particles escape the BH kernel and wind launching covers the whole solid angle, irrespective of anisotropy. On the other hand, the kinetic energy injection feedback model employed in this paper would be prone to generate stronger feedback, due to the delayed wind thermalization intrinsic to this approach, than achieved via launching spawned wind particles. It is therefore not obvious how and by how much bubble formation and MBHs dynamics would differ due to using these different feedback subgrid models. We will address this issue in future works.

ACKNOWLEDGEMENTS

We acknowledge the CINECA award under the ISCRA initiative, for the availability of high-performance computing resources and support (project number HP10CJ7AUZ). The analyses reported in this work have been mainly performed using pynbody (Pontzen et al. 2013). AL, MD, and FH acknowledge funding from MIUR (Ministero dell'Istruzione e del Merito) under the grant PRIN 2017-MB8AEZ.

DATA AVAILABILITY

The data underlying this article will be shared on reasonable request to the corresponding author.

REFERENCES

Amaro-Seoane P. et al., 2022, preprint (arXiv:2203.06016)
Anglés-Alcázar D., Davé R., Faucher-Giguère C.-A., Özel F., Hopkins P. F., 2017, MNRAS, 464, 2840
Bardeen J. M., Petterson J. A., 1975, ApJ, 195, L65
Barnes J. E., 2002, MNRAS, 333, 481
Barnes J. E., Hernquist L. E., 1991, ApJ, 370, L65
Barnes J. E., Hernquist L., 1996, ApJ, 471, 115
Begelman M. C., Blandford R. D., Rees M. J., 1980, Nature, 287, 307
Blumenthal K. A., Barnes J. E., 2018, MNRAS, 479, 3952
Bogdanović T., Reynolds C. S., Miller M. C., 2007, ApJ, 661, L147
Bondi H., 1952, MNRAS, 112, 195
Bondi H., Hoyle F., 1944, MNRAS, 104, 273
Bonetti M., Bortolas E., Lupi A., Dotti M., Raimundo S. I., 2020, MNRAS, 494, 3053
Campitiello S., Ghisellini G., Sbarrato T., Calderone G., 2018, A&A, 612, A59
Capelo P. R., Dotti M., 2017, MNRAS, 465, 2643
Cenci E., Sala L., Lupi A., Capelo P. R., Dotti M., 2021, MNRAS, 500, 3719(C21)
Chandrasekhar S., 1943, ApJ, 97, 255
Colpi M., Dotti M., Mayer L., Kazantzidis S., 2007, preprint (arXiv:0710.5207)
Costa T., Pakmor R., Springel V., 2020, MNRAS, 497, 5229
Curtis M., Sijacki D., 2016, MNRAS, 463, 63
De Rosa A. et al., 2019, New Astron. Rev., 86, 101525
Dotti M., Colpi M., Haardt F., 2006, MNRAS, 367, 103
Dotti M., Colpi M., Haardt F., Mayer L., 2007, MNRAS, 379, 956
Dotti M., Ruszkowski M., Paredi L., Colpi M., Volonteri M., Haardt F., 2009, MNRAS, 396, 1640
Dotti M., Volonteri M., Perego A., Colpi M., Ruszkowski M., Haardt F., 2010, MNRAS, 402, 682
Downes D., Solomon P. M., 1998, ApJ, 507, 615
eLISA Consortium et al., 2013, preprint (arXiv:1305.5720)
Escala A., Larson R. B., Coppi P. S., Mardones D., 2005, ApJ, 630, 152
Fiacconi D., Sijacki D., Pringle J. E., 2018, MNRAS, 477, 3807
Gruzinov A., Levin Y., Matzner C. D., 2020, MNRAS, 492, 2755
Hernquist L., 1989, Nature, 340, 687
Hernquist L., 1990, ApJ, 356, 359
Hopkins P. F., 2015, MNRAS, 450, 53
Hopkins P. F., Quataert E., 2011, MNRAS, 415, 1027
Hoyle F., Lyttleton R. A., 1939, Math. Proc. Camb. Phil. Soc., 35, 405
King A. R., Lubow S. H., Ogilvie G. I., Pringle J. E., 2005, MNRAS, 363, 49
Li X., Chang P., Levin Y., Matzner C. D., Armitage P. J., 2020, MNRAS, 494, 2327
Lodato G., Pringle J. E., 2007, MNRAS, 381, 1287
Lupi A., Haardt F., Dotti M., 2015, MNRAS, 446, 1765
Masset F. S., 2017, MNRAS, 472, 4204
Masset F. S., Velasco Romero D. A., 2017, MNRAS, 465, 3175
Mayer L., Kazantzidis S., Madau P., Colpi M., Quinn T., Wadsley J., 2007, Science, 316, 1874
Mihos J. C., Hernquist L., 1996, ApJ, 464, 641
Ostriker E. C., 1999, ApJ, 513, 252
Pontzen A., Roškar R., Stinson G., Woods R., 2013, Astrophysics Source Code Library, record ascl:1305.002
Sala L., Cenci E., Capelo P. R., Lupi A., Dotti M., 2021, MNRAS, 500, 4788(S21)
Sanders D. B., Mirabel I. F., 1996, ARA&A, 34, 749
Shakura N. I., Sunyaev R. A., 1973, A&A, 500, 33
Sijacki D., Springel V., Haehnelt M. G., 2011, MNRAS, 414, 3656
Souza Lima R., Mayer L., Capelo P. R., Bellovary J. M., 2017, ApJ, 838, 13
Springel V., Di Matteo T., Hernquist L., 2005, MNRAS, 361, 776
Torrey P. et al., 2020, MNRAS, 497, 5292
Toyouchi D., Hosokawa T., Sugimura K., Kuiper R., 2020, MNRAS, 496, 1909
Tremmel M., Karcher M., Governato F., Volonteri M., Quinn T. R., Pontzen A., Anderson L., Bellovary J., 2017, MNRAS, 470, 1121
Volonteri M., Gültekin K., Dotti M., 2010, MNRAS, 404, 2143
Wang L., Li X., 2022, ApJ, 932, 108

APPENDIX A: CONVERGENCE

In order to discuss the convergence of our results we performed additional simulations, with both smaller and higher resolution, in the cases **f_nofb** and **f_a**. In particular, we sampled the CND with 10^5, $3 \cdot 10^5$, and $3 \cdot 10^6$ gas particles, in addition to the 10^6 case presented in Section 4.1. For all these resolutions the number of star particles is five times that of the gas. Fig. A1 shows how the evolution of the MBHs separation in **f_nofb** changes with resolution and reveals that the dynamics converges by increasing the number of particles. On the other hand, we do not expect convergence in simulations with feedback due to the stochastic nature of our subgrid feedback model. Indeed, depending on which gas particles receive a kick at a given time-step, the resulting bubbles can display morphological differences, such that their cumulative effect in time can lead to very different trajectories, i.e. different realizations of the same stochastic process (see Fig. A2 for the **f_a** case).

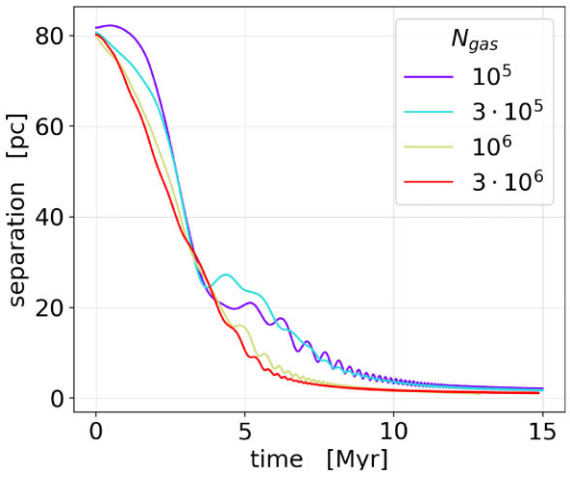

Figure A1. Time evolution of the MBHs separation for different resolutions in the case **f_nofb**.

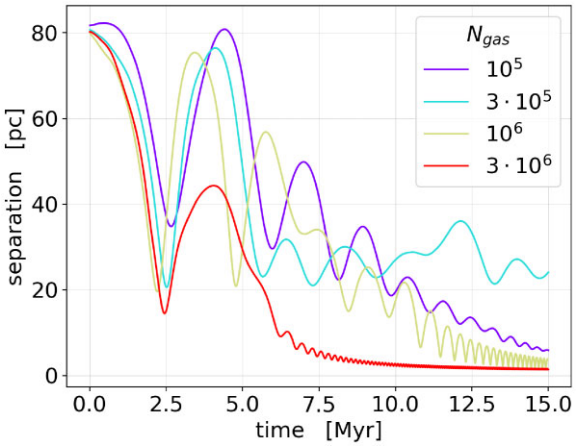

Figure A2. Time evolution of the MBHs separation for different resolutions in the case **f_a**.

APPENDIX B: FORCE SOFTENING

The weighting function w appearing in the definition of the anisotropy vector (equation 7) is defined as the force softening function used in GIZMO (see equation H6 in Hopkins 2015), i.e. $w(r) \equiv h^{-1}\mathrm{d}\phi(q;\, h)/\mathrm{d}q$ where $h = 2.8 \times \epsilon_{\mathrm{soft,\,BH}}$ is the force softening length, $q = r/h$ and

$$\phi(q;h) = -\frac{1}{qh} \times \begin{cases} \frac{14}{5}q - \frac{16}{3}q^3 + \frac{48}{5}q^5 - \frac{32}{5}q^6, & 0 \le q < 0.5 \\ -\frac{1}{15} + \frac{16}{5}q - \frac{32}{3}q^3 + 16q^4 - \frac{48}{5}q^5 + \frac{32}{15}q^6, & 0.5 \le q < 1 \\ 1, & q \ge 1. \end{cases} \tag{B1}$$

APPENDIX C: ANGULAR DISTRIBUTIONS

In Figs C2 and C1, we report the histograms of the quantity θ for **e** and **q** simulations. As pointed out in Section 4.4, the distribution of θ, peaked at small angles ($<\pi/2$) in **nofb** simulations, spreads over the whole range $[0, \pi]$ when feedback is turned on, due to the presence of low-density bubbles trailing the MBH, which tend to accelerate it, hampering DF. We note that the simulations in which the peak of the distribution is more shifted to the right (i.e. more frequent feedback acceleration) are **q_iso** and **q_a**, which are also the only two simulations whose orbits do not decay over the simulated time.

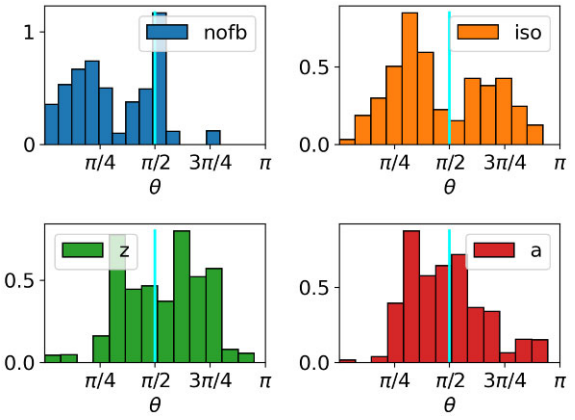

Figure C1. Histograms of θ in **e** simulations.

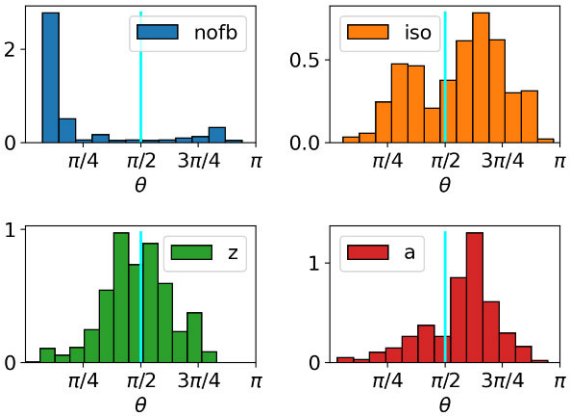

Figure C2. Histograms of θ in **q** simulations.

This paper has been typeset from a TEX/LATEX file prepared by the author.